Shahrood University of Technology

Journal of Mining and Environment (JME)

Journal homepage: www.jme.shahroodut.ac.ir

Iranian Society of Mining Engineering (IRSME)

Three-Dimensional Inversion and Interpretation of Ground Magnetic Data to Map Iron Resources: a Case Study of Shavaz Iron Ore in Iran

Bardiya Sadraeifar[1], Maysam Abedi[2]*, and Seyed Hossein Hosseini[1]

1. Institute of Geophysics, University of Tehran, Tehran, Iran
2. School of Mining Engineering, College of Engineering, University of Tehran, Tehran, Iran

Article Info

Received 20 June 2024
Received in Revised form 1 October 2024
Accepted 30 November 2024
Published online 30 November 2024

DOI: 10.22044/jme.2024.14679.2775

Keywords

Shavaz
Magnetite
Susceptibility inversion
Synthetic model
Analytic signal

Abstract

The Shavaz iron deposit, located in the southwest Yazd province in Central Iranian Block, near The Bafq metallogenic belt, is a significant and economically valuable iron oxide-apatite resource. It features hematite and a minor content of magnetite, detectable through potential field geophysical surveys. This study aimed to target magnetite mineralization within the deposit using constrained susceptibility inversion. We began by simulating a multi-source synthetic model with three identical cubes at different depths to evaluate the sparse norm inversion approach. The method was then applied to the case study after the essential magnetic data corrections. To refine the interpretation of residual magnetic anomalies and gain insights into their source and depth, the analytic signal and upward continuation methods were employed. Inversion results across different cross-sections revealed two distinct, shallow, lens-shaped magnetite mineralizations with an average vertical extent of 60 meters. Notably, one magnetite body lies approximately 30 meters deeper due to the Dehshir-Baft fault influence. Low normalized mis-fit values confirmed the successful minimization of the objective function during inversion. Additionally, the reconstructed susceptibility models align well with the previous geological studies and borehole data, demonstrating the efficiency of the sparse norm inversion algorithm.

1. Introduction

Advanced geophysical surveys, particularly through improvements in the inversion and modeling, are revolutionizing mineral exploration by enabling detailed imaging of subsurface resources. The Oldenburg and Pratt categorized inversion methods for mineral and natural resource exploration into three groups [1]:

1. Discrete body inversion: Efficiently models the simple structures with minimal computational requirements, making it ideal for the initial assessments. This method does not incorporate the geological and lithological data [1-2].
2. Pure property inversion: Requires detailed discretization and powerful computers for a complex modeling. This method allows for the inclusion of bound constraints and depth weighting terms in the inversion formulation, making it suitable for research and industrial applications [1, 3-6].
3. Petrophysical/lithological inversion: Incorporates the geological and petrophysical data for more relevant models, but is limited by the data availability [7-9].

This categorization highlights the trade-off between computational cost, model detail, and geological relevance, when choosing the most suitable inversion technique.

This introduction focuses on a particular pure property inversion method was utilized in this study, for iron deposit exploration. Due to the presence of hematite and magnetite, iron deposits like Banded Iron Formations (BIFs), Iron Oxide-Apatite (IOA) deposits, and Kiruna-type deposits are prime targets for the gravity and magnetic methods [10-11]. Magnetite's strong ferromagnetic

Corresponding author: maysamabedi@ut.ac.ir (M. Abedi)

nature makes it detectable through airborne and ground magnetic surveys. However, successful exploration depends on selecting the right inversion method. For deposits with weak remnant magnetization, susceptibility inversion, which ignores remanence, is a fast and common choice for the academic and industrial projects, due to its simplicity [12-14]. For deposits with a significant remnant magnetization, Magnetization Vector Inversion (MVI) is more accurate, as it recovers total magnetization including both the induced and remnant components [15-17].

This study utilizes 3D sparse norm susceptibility inversion for magnetite targeting. Although the Magnetization Vector Inversion (MVI) method offers a higher accuracy, susceptibility inversion remains a valuable tool for the initial inverse modeling. We implemented a constrained inversion by defining the upper and lower bounds based on the geological observations and borehole data. This approach guided the inversion toward a geologically realistic solution, resembling the actual subsurface conditions.

Magnetite mineralization typically features sharp boundaries, and is not continuously distributed, presenting a significant challenge for the traditional inversion methods. The Tikhonov inversion, which tends to produce smooth models, is unsuitable in this context, because it cannot accurately recover the models with sharp boundaries and distinct depth variations. To address this limitation, we employ a sparse norm inversion technique. This method is specifically designed to overcome the inherent smoothness constraint of the Tikhonov inversion, enabling us to achieve a more precise and realistic interpretation of the subsurface structure. Sparse norm inversion enhances the resolution of sharp boundaries, and accurately delineates the distribution and depth of magnetite mineralization, leading to improved geological and geophysical insights.

Although the Shavaz deposit is not as large as the major iron resources in Iran such as the Gol-e-Gohar complex or the iron deposits in the Bafq metallogenic belt, it is considered as an economic iron deposit containing significant hematite and a small portion of magnetite [18]. Hematite mineralization is mostly detectable through gravity surveys, due to its high density contrast and weak magnetization, while the magnetic methods are more efficient for detecting magnetite. Several significant studies have been conducted on the Shavaz iron deposit, providing valuable and informative insights [19-22]. However, in this study, we employ a sparse norm inversion in a mixed L_p norm framework to promote sparsity in the reconstructed susceptibility models for a more accurate recovery of the depth and geometry of the magnetite mineralization.

In the following sections, we begin by discussing the susceptibility inversion method and its underlying mathematical principles. Subsequently, a synthetic model is simulated to evaluate the inversion's effectiveness in recovering the structures at varying depths. Following this evaluation, the geological context of the studied area and the geophysical surveys conducted are presented. Finally, the inversion results are interpreted, and the efficiency of the inversion algorithm for the real-world case study is assessed. A subsequent section will address the geological correlation, and conclusions derived from this work. Notably, both the forward and inverse modelings were performed using the SimPEG framework, a well-established Python library for geophysical modeling [23].

2. Methodology

In this section, we discuss the sparse norm inversion methodology used within the SimPEG framework to generate the susceptibility contrast models for synthetic modeling and case study. We used the mixed L_p norm inversion approach [24] to recover subsurface physical properties, as discussed in this section. We begin by formulating the forward problem as follows [24-25]:

$$\boldsymbol{b}^{obs} = \mathbf{Fm} \tag{1}$$

In the above equation, $\boldsymbol{b}^{obs}$ is the vector of magnetic observations, and $\mathbf{m}$ is the magnetization of the prisms (cells) in the discretized environment, as shown below [25]:

$$\begin{aligned} \boldsymbol{b}^{obs} &= [b^x, b^y, b^z]^T \\ \boldsymbol{m} &= [M^x, M^y, M^z]^T \end{aligned} \tag{2}$$

In Equation 1, $\mathbf{F}$ is the forward operator, a matrix that produces the geophysical data based on the physical properties (magnetization). It is important to note that Equation 1 is based on the following descriptions (Equation 3), where M represents the number of cells in the discretized environment, and N represents the number of data points or observations [24]:

$$\mathbf{m} \in \mathbb{R}^{3M}, \boldsymbol{b}^{obs} \in \mathbb{R}^{N}, \boldsymbol{F} \in \mathbb{R}^{N \times 3M} \tag{3}$$

The Li and Oldenburg define geophysical inverse problems, as an optimization problem, which is generally formulated as follows [3-6]:

$$\min \phi(m) = \phi_d + \beta \phi_m \quad (4)$$

In a brief explanation, $\phi(m)$ serves as the model's objective function, comprising two key elements: the data mis-fit term (ϕ_d), which measures how well the model m explains the observed geophysical data, and the regularization term (ϕ_m), which control the complexity of the model by imposing constraints [5]. ϕ_d is defined as the sum of squared differences between the observed data ($\boldsymbol{d}_i^{obs}$), and the predicted data ($\boldsymbol{d}_i^{pred}$) typically expressed as follows [24]:

$$\phi_d = \sum_{i=1}^{N} \left(\frac{\boldsymbol{d}_i^{pred} - \boldsymbol{d}_i^{obs}}{\boldsymbol{\sigma}_i} \right)^2 = \|\mathbf{W}_d(\mathbf{Fm} - \mathbf{d}^{obs})\|_2^2 \quad (5)$$

Here, $\boldsymbol{\sigma}_i$ represents the estimated uncertainty or standard deviation associated with each data point. $\mathbf{W}_d$ denotes a weighted diagonal matrix, reflecting the inverse of the uncertainties. **F** is a matrix that relates the model parameters **m** to the predicted data ($\boldsymbol{d}_i^{pred}$). This formulation quantifies the discrepancy between the observed and predicted data, considering the uncertainties $\boldsymbol{\sigma}_i$ with each observation [3-5, 24].

In the context of the regularization term, its common formulation as an L_2 norm is represented as follows [3, 24]:

$$\phi_m = \alpha_s \phi_s + \alpha_x \phi_x + \alpha_y \phi_y + \alpha_z \phi_z = \sum_{r=s,x,y,z} \alpha_r \left\| \mathbf{W}_r \mathbf{V}_r \mathbf{G}_r (\mathbf{m} - \mathbf{m}^{ref}) \right\|_2^2 \quad (6)$$

ϕ_s is the smallness term, and $\phi_{x,y,z}$ are the roughness terms. The smallness term measures how much the model deviates from a reference model. Essentially, it encourages the model parameters to stay close to pre-defined values. The roughness terms, on the other hand, measure the smoothness of the model along different directions (typically the Cartesian directions x, y, and z). These terms use gradient operators to quantify changes or variations in the model parameters across space, promoting smoother transitions and discouraging abrupt changes. Together, the smallness and roughness terms help to prevent overfitting, ensure stability, and guide the model towards realistic solutions by incorporating prior knowledge and enforcing smoothness [5].

The matrices $\mathbf{W}_{r(s,x,y,z)}$, $\mathbf{V}_{r(s,x,y,z)}$, and $\mathbf{G}_{r(s,x,y,z)}$ play crucial roles in the regularization of a model's objective function. $\mathbf{W}_{r(s,x,y,z)}$ are weighting matrices that apply specific weights to different parts of the model or data, reflecting their varying importance or reliability. $\mathbf{V}_{r(s,x,y,z)}$ are volume weighting matrices that normalize the contributions of different model cells based on their size, ensuring balanced representation. $\mathbf{G}_{r(s,x,y,z)}$ are gradient operators that measure the spatial derivative from the model parameters, promoting smoothness by capturing how parameters vary across space. Together, these matrices help prevent overfitting, maintain stability, and guide the model towards realistic solutions by incorporating prior knowledge and enforcing smoothness.

In a mixed L_p norm condition [16, 24, 26-27], the regularization term can be writen as follows, where $0 \leq p \leq 2$:

$$\phi_m^p = \alpha_s \phi_s^p + \alpha_x \phi_x^p + \alpha_y \phi_y^p + \alpha_z \phi_z^p = \alpha_s \|\mathbf{W}_s \mathbf{V}_s \mathbf{R}_s(\mathbf{m})\|^p + \sum_{r=x,y,z} \alpha_r \|\mathbf{W}_r \mathbf{V}_r \mathbf{R}_r \boldsymbol{G}_r(\mathbf{m})\|^p \quad (7)$$

The first component in the regularization ($\alpha_s \|\mathbf{W}_s \mathbf{V}_s \mathbf{R}_s(\mathbf{m})\|^p$) is the model smoothness term. In this term, α_s is the regularization parameter, $\mathbf{W}_s$ is weighting matrix for the smoothness term, which can adjust the importance of different parts of the model. $\mathbf{V}_s$ is the scaling matrix for the model parameters, and $\mathbf{R}_s$ is the regularization operator that enforces smoothness on the model **m** . The second component ($\alpha_s \|\mathbf{W}_s \mathbf{V}_s \mathbf{R}_s(\mathbf{m})\|^p$) is the gradient term. These terms ensure that the model gradients (change in the model parameters) in the x, y, and z directions are smooth or sparse, and do not exhibit large fluctuations. Each direction can be weighted differently to account for anisotropy in the model. All the parameters in the smoothness term can similarly be defined from the gradient term [24, 27].

In a condition where we have $\phi_m^p = \alpha_s \phi_s^0 + \alpha_x \phi_x^2 + \alpha_y \phi_y^2 + \alpha_z \phi_z^2$, this norm combination is called the sparse norm in the SimPEG framework [24, 26, 28-29]. This norm combination, as used in this study, produces models with sharper contrasts between different geological units, making it easier to identify distinct boundaries.

3. Synthetic Scenarios

This section evaluates the effectiveness of the inversion methodology in recovering a synthetic model containing three identical cubes. The synthetic environment extends approximately 320 meters in both the x and y directions, ranging from -160 meters to 160 meters. Vertically, it extends from -160 meters to 0. To accurately assess the inversion method's efficiency, a dense data spacing was chosen within the synthetic environment. The data spacing was set to 10 meters, resulting in a total of 1,024 data points collected.

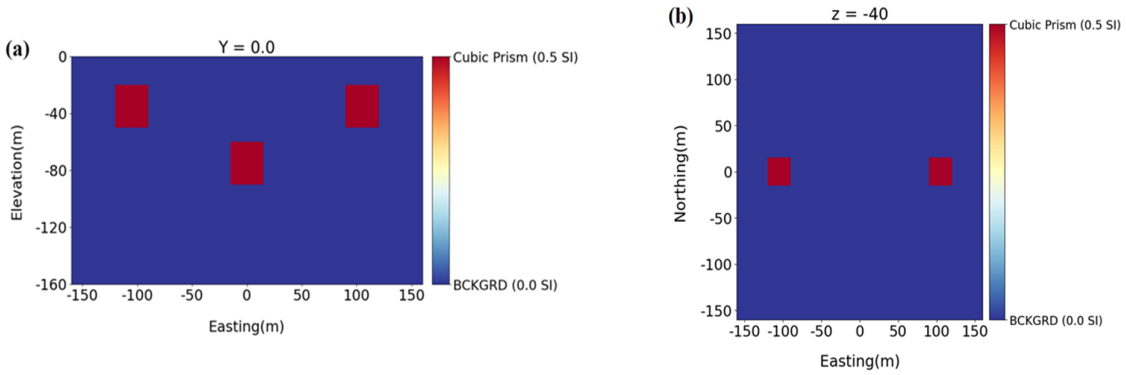

Figure 1. Synthetic model with three identical cubes having the same magnetic susceptibility (0.5 SI). (a) xz cross-section at y = 0, (b) Plan view at depth = -40 m.

To discretize the synthetic subsurface environment, tensor meshing was employed [23]. In this type of meshing, all the cells are similar to each other, but we have the ability to change the cell length in each of the three directions. However, in this synthetic study, all cells have the same dimensions of 5 × 5 × 5 meters. We considered the cell dimensions to be smaller than the synthetic data spacing to represent the models using fine meshes. Figure 1 illustrates the synthetic modeling in an xz cross-section (Figure 1(a)) and a plan view of the model (Figure 1(b)). The synthetic model includes three cubes, each measuring 30 × 30 × 30 meters, with one cube located 40 meters deeper than the others. All three cubes have a magnetic susceptibility of 0.5 SI without remanent magnetization.

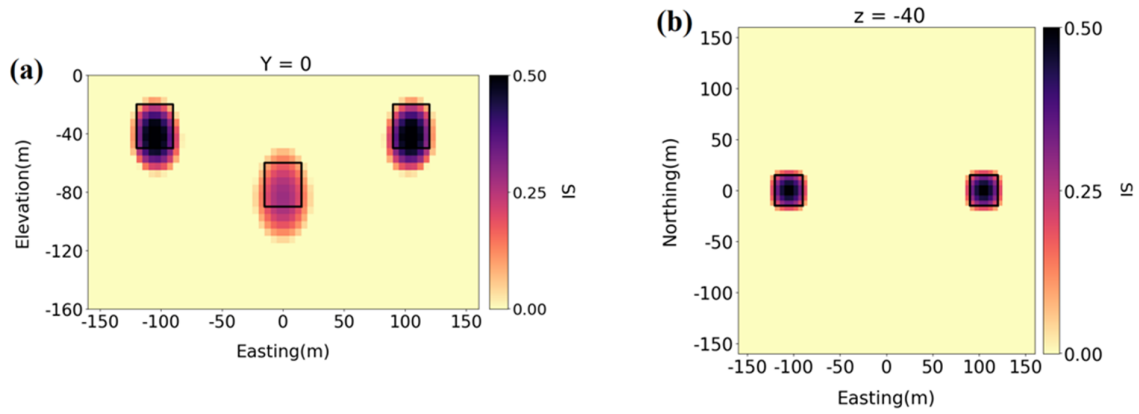

Figure 2. Inversion results for the synthetic model after 30 iterations. (a) xz cross-section of the recovered model at y = 0, (b) Plan view of the recovered model at a depth of -40 m. The inversion algorithm successfully recovered the three cubes at different depths, demonstrating its ability to reconstruct both the shallow and deep features.

Figure 2 shows the inversion results. The sparse norm inversion successfully recovered three cubes with sharp boundaries. Figure 3 compares the observed and predicted anomalies. Figure 3(a) shows the observed anomalies from the synthetic model with 2% Gaussian noise. Figure 3(b) shows the anomalies from the recovered models. Figure 3(c) shows the normalized residual, representing the weighted difference between the observed and predicted data.

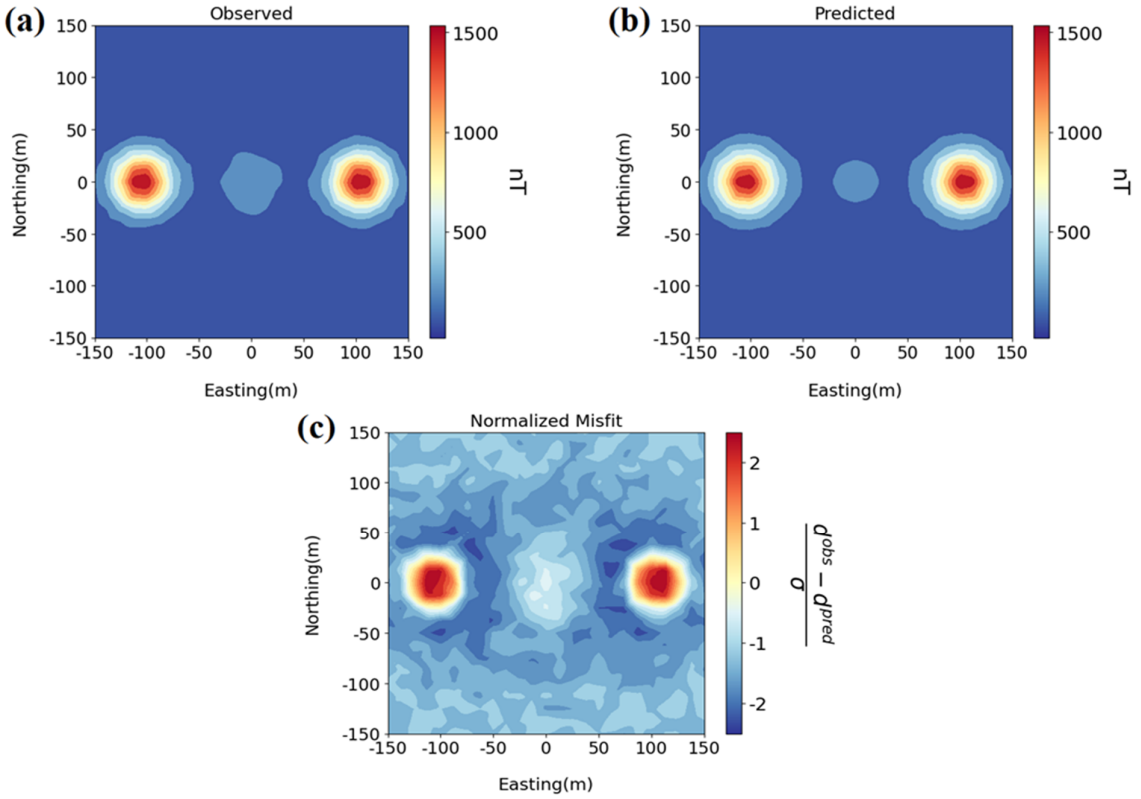

Figure 3. Anomalies resulted from the true and recovered models and their differences. (a) Magnetic anomalies from the synthetic model, (b) Magnetic anomalies from the recovered model after inversion, (c) Weighted normalized residuals, showing the difference between the observed and predicted data. Positive values indicate the true model has a stronger magnetic anomaly than the recovered model, and negative values indicate the opposite.

Figure 4 represents the convergence curve for the synthetic model inversion, and shows the progression of the inversion algorithm, as it iteratively updates the model parameters to fit the observed data. The objective function related to the data mis-fit (ϕ_d) is minimized effectively within the first 5 iterations, suggesting that the algorithm quickly finds a model that fits the observed data well. The increase and subsequent stabilization of ϕ_m^p around 70 suggests a significant role of regularization or constraint enforcement in the inversion process. The initial increase reflects the adjustment of model parameters, and the stabilization indicates that a balance has been achieved between the data fitting and regularization.

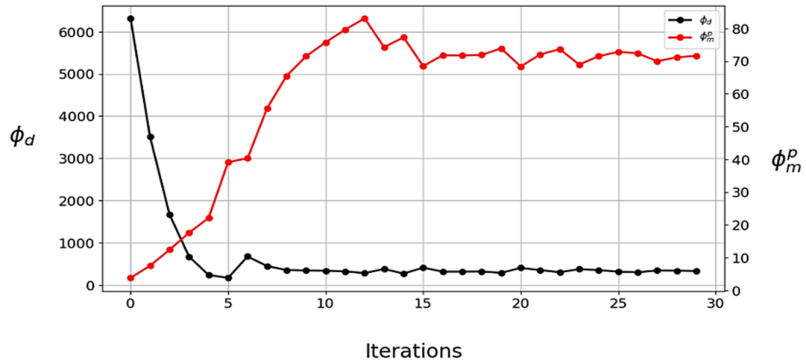

Figure 4. Convergence curve for the inversion of the synthetic data. The x-axis shows the number of iterations, indicating how many steps it took for the inversion to reach the stopping criteria. The left y-axis shows the mis-fit (ϕ_d), which was minimized over 30 iterations. The right y-axis shows the model norm variations (ϕ_m^p) over different iterations.

4. Real Case Study

In this section, we first discuss about the geological context of the Shavaz deposit. In the next part, we discuss about the geophysical surveys and interpreted the magnetic anomalies through analytic signal and upward continuation, and in the final part, we discuss about the inversion results and susceptibility models.

4.1. Geological Setting

Iran, situated on the Iranian plateau, has witnessed a dynamic geological history characterized by numerous transformative events. The country is divided into several structural geological zones based on their tectonic setting, petrological characteristics, volcanism, orogenic events, and seismic activities [30]. This classification includes Central Iran, Sanandaj-Sirjan Zone (SSZ), Alborz, Zagros, Makran, East Iran Zone, Kopeh Dagh, and Lut Block [30-33]. Analysis of the Iranian magmatism and structural features has revealed the existence of six major metallogenic phases, spanning a vast timeframe from the Late Proterozoic era to the Quaternary. Within these metallogenic phases, iron mineralization occurred during four key periods [30]:

1. Late Proterozoic-early Cambrian iron mineralization: This phase, the most abundant includes deposits with the volcano-sedimentary and orthomagmatic origins.
2. Paleozoic-early Triassic iron mineralization: These deposits are less abundant, smaller in size, and have a lower iron grade compared to the earlier phase.
3. Mesozoic iron mineralization: The Sanandaj-Sirjan Zone became a hotspot for iron mineralization during this era, with the primary deposit type being skarn, often containing associated manganese.
4. Cenozoic iron mineralization: primarily found in the Urumiyeh-Dokhtar Zone and Alborz, with significant skarn deposits.

The most economically valuable iron resources in Iran originated during the late Proterozoic-early Cambrian and the late Eocene to Pliocene (Cenozoic) [21]. The Bafq metallogenic belt, which is located in the Kashmar-Kerman arc, is the most significant zone for iron mineralization, containing over 2 billion tons of iron ore. These deposits share common properties such as age, host rock alteration, presence of apatite, and volcanic-magmatic origins [30].

The Shavaz iron deposit, located within Iran's Central Iranian block southwest of the Yazd province, near the Bafq mining district, spans an area of 550 × 650 m² [18]. This deposit, influenced by the Nain-Dehshir-Baft fault zone, is notable for its significant metal potential. The iron ore, predominantly composed of hematite with minor magnetite, is found in proximity to volcanic rocks and tuffs. This spatial association suggests that the hydrothermal processes stemming from volcanic activity played a crucial role in the iron deposition [22]. The oldest rocks in the area are the Cretaceous granite and granodiorites of the Shirkuh complex, located to the east of the deposit. These intrusive rocks range primarily from granodiorite to granite. Studies indicate that the Shirkuh rocks initially formed as biotite-bearing granodiorites, and subsequently evolved to become more acidic [33]. Figure 5 presents the geological map of the area, which is covered by Neogene sediments and Quaternary alluviums.

The Sangestan formation, a significant geological unit in the region, comprises alternating layers of sandstone, fine-grained conglomerate, and red marls interspersed with limestone. Its lower boundary exhibits an unconformable relationship with the underlying Shirkuh granites [33-35]. While the precise age of the Sangestan formation remains a subject of debate, the Geological Organization of Iran attributes it to the lower Cretaceous period [33]. Overlying these lower Cretaceous sediments in the Yazd region is the Taft formation, characterized by dolomitic limestone. Microfossil analyses suggest that the Taft formation also dates to the Cretaceous period [35]. This formation initiates with shale and thin limestone beds, which transition into thicker limestone beds at higher stratigraphic levels, thereby contributing to the region's pronounced topography. Additionally, these limestones are periodically inter-layered with black limestone strata [35].

4.2. Geophysical survey

A ground magnetic survey was conducted in the studied area using a proton magnetometer in 2010 [21, 35]. The collected data underwent several processing steps:

1. Diurnal correction: Diurnal variations, natural fluctuations in the Earth's magnetic field throughout the day, were removed from the data.
2. IGRF removal: The influence of the Earth's main magnetic field, modeled by the International Geomagnetic Reference Field (IGRF), was

eliminated. Adjustments were made for the local declination (3.2 degrees) and inclination (49.2 degrees) angles.

3. Reduction To Pole (RTP) transformation: This filter normalized the data for geometric effects caused by the Earth's magnetic field, effectively placing all measurements at the magnetic poles for easier analysis.

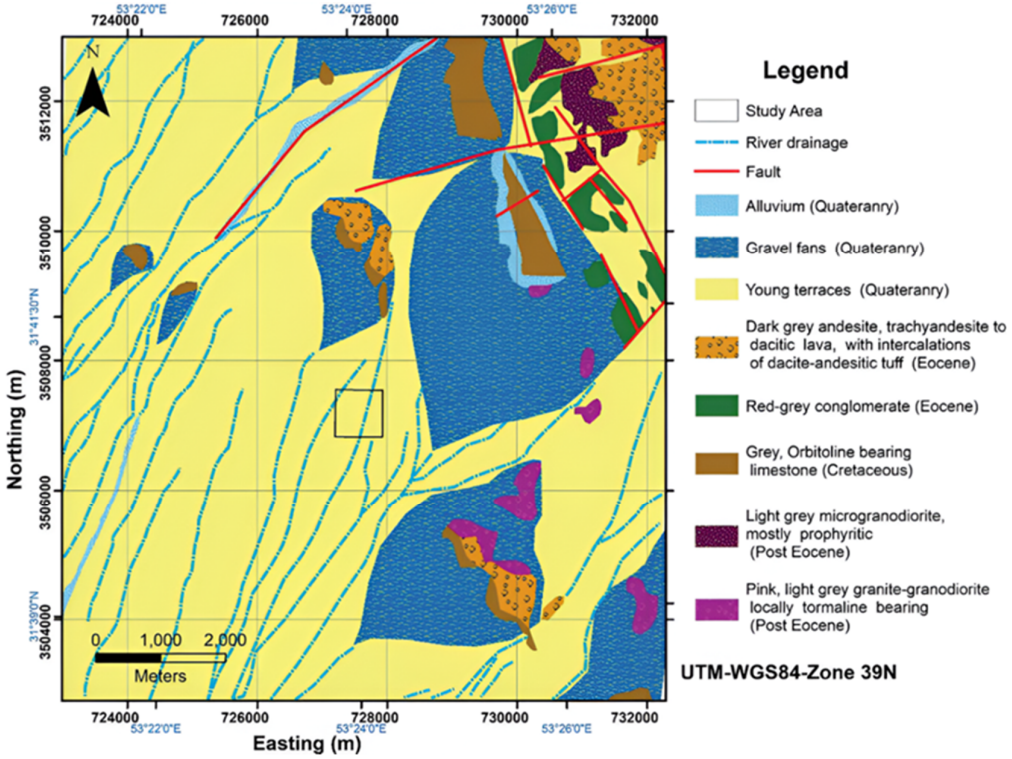

Figure 5. Geological map of the Shavaz deposit [36]. The map depicts the geological setting of the studied area, highlighting faults, lithological units, and the location of the Shavaz iron deposit. The surrounding region is predominantly underlain by sedimentary rocks (Quaternary terraces) including conglomerates, sandstones, and travertine.

The survey employed a north-south line grid with 20-meter line spacing and station spacing of typically 10 meters (occasionally 20 meters). This resulted in a total of 1641 data points collected across an area of approximately 550 meters by 650 meters [21, 35]. Figure 6(a) displays the Total Magnetic Intensity (TMI) map of the studied area after applying corrections. Figure 6(b) shows the results of applying an analytic signal filter to the TMI data. This filter enhances the boundaries (edges) of magnetic anomalies, allowing for a better differentiation of individual causative sources. Figure 6(c) presents the magnetic anomalies after a 40-meter upward the continuation process. This process reduces the influence of shallow magnetic sources, aiding in the identification of deeper anomalies.

In the context of interpreting the observations, The Total Magnetic Intensity (TMI) anomaly map (Figure 6(a)) reveals significant magnetic anomalies with a prominent high around coordinates (727500, 3507300), indicating the presence of a major magnetite body near the surface. This high magnetic intensity is consistent with the expected response from a dense and magnetically susceptible mineral deposit, suggesting a significant target for exploration. Additionally, a smaller low-intensity anomaly around coordinates (727600, 3507050) hints at a secondary magnetic source, potentially a smaller or less magnetized body, which may warrant further investigation.

The Analytic Signal (AS) map (Figure 6(b)) complements the TMI data by providing a clear depiction of the edges of magnetic bodies, regardless of their magnetization direction. The highest amplitude in the AS map, centered at (727500, 3507300), corroborates the presence of the primary magnetic source identified in the TMI map. This map also reveals additional high-amplitude zones, around (727750, 3507400), and

(727600, 3507050), suggesting the presence of smaller magnetic bodies.

The upward continuation map (Figure 6(c)), calculated at 40 meters above the ground surface, smooths out the near-surface anomalies to emphasize deeper sources. This map reinforces the presence of a significant magnetic source around (727500, 3507300), as seen in the TMI and AS maps, suggesting that the primary magnetite body extends to greater depths. The overall trend indicates a prominent deep-seated magnetic source in the north-central part of the map, with a potential secondary source to the south around (727600, 3507050).

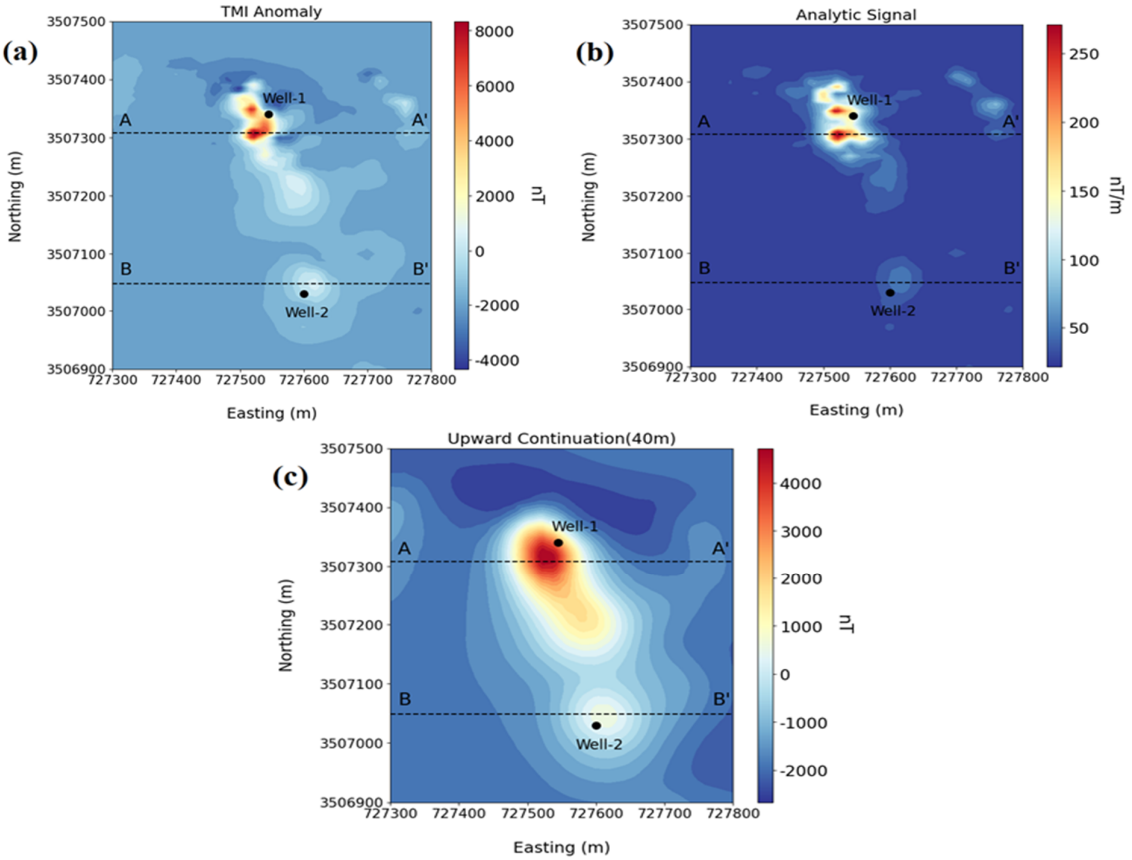

Figure 6. (a) Total Magnetic Intensity (TMI) map following corrections for diurnal variations, International Geomagnetic Reference Field (IGRF), and reduction to the pole, (b) Analytic signal map, (c) Upward continuation map (40 m). The locations of the drilling wells are also indicated.

4.3. Inversion results

For performing the inversion on the field data, we first discretized the environment into the 60 × 70 × 40 cells along the x, y, and z directions, respectively. Based on the analysis of geological and geophysical data from the previous studies [18, 19, 21, 22, 34, 35], the upper bounds were set at 1.0 SI. The inversion algorithm converged after 30 iterations, reaching a pre-defined stopping criterion. This criterion, known as the chi-square factor ($\chi^2 = 1$), indicates that the inversion aimed to achieve a data mis-fit equivalent to the estimated noise level in the magnetic data, assuming a chi-squared distribution of the mis-fit values. Figure 7 presents the inversion results along the profiles (AA' and BB') displayed in Figure 6. The inversion results for the profile AA' (Figure 7(a)) suggest a lens-shaped magnetic body extending approximately 60-70 meters vertically. In contrast, the inversion results for profile BB' ((Figure 7(b)) reveal a deeper causative magnetic source with approximately the same vertical extent and a slightly weaker susceptibility.

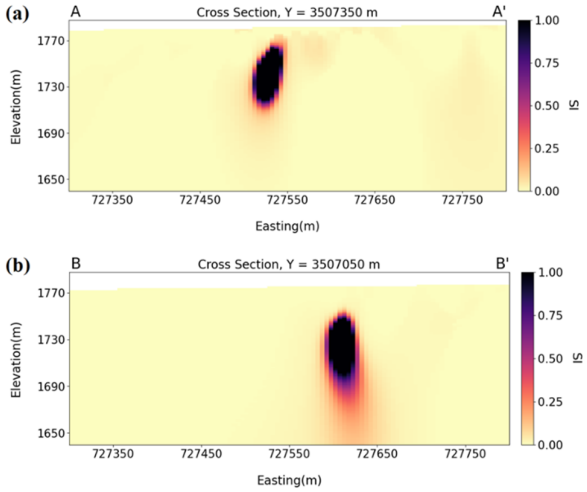

Figure 7. Plan view of the inversion results at different depths, revealing the distribution of the magnetized ore body. (a) Susceptibility model at elevation = 1708 m, (b) elevation = 1727 m, (c) Elevation = 1744 m, and (d) Elevation = 1759 m.

Figure 8 presents the inversion results at different depths. As shown, when moving from a depth of 1708 m (Figure 8(a)) to 1759 m (Figure 8(d)), the secondary source located around (727600, 3507050) disappears, while the primary source located around (727500, 3507300) becomes amplified. These observations align well with the inversion results in Figure 8, and validate that the primary source has a higher magnetic susceptibility at a shallower depth compared to the secondary source. Their separation may be the result of the Nain Dehshir-Baft fault.

Figure 9 analyzes the difference between the observed and predicted magnetic anomalies. Figure 9(a) shows the Total Magnetic Intensity (TMI) anomaly after corrections (refer to Figure 6(a)), while Figure 9(b) displays anomalies derived from the inverted model. Figure 9(c) presents the normalized residual, similar to Figure 3(c), representing the weighted difference between the observed and predicted data. While the inversion successfully recovered anomalies in critical zones, there's a potential for improvement. Future studies could utilize a magnetization vector inversion method to achieve a potentially a more accurate model.

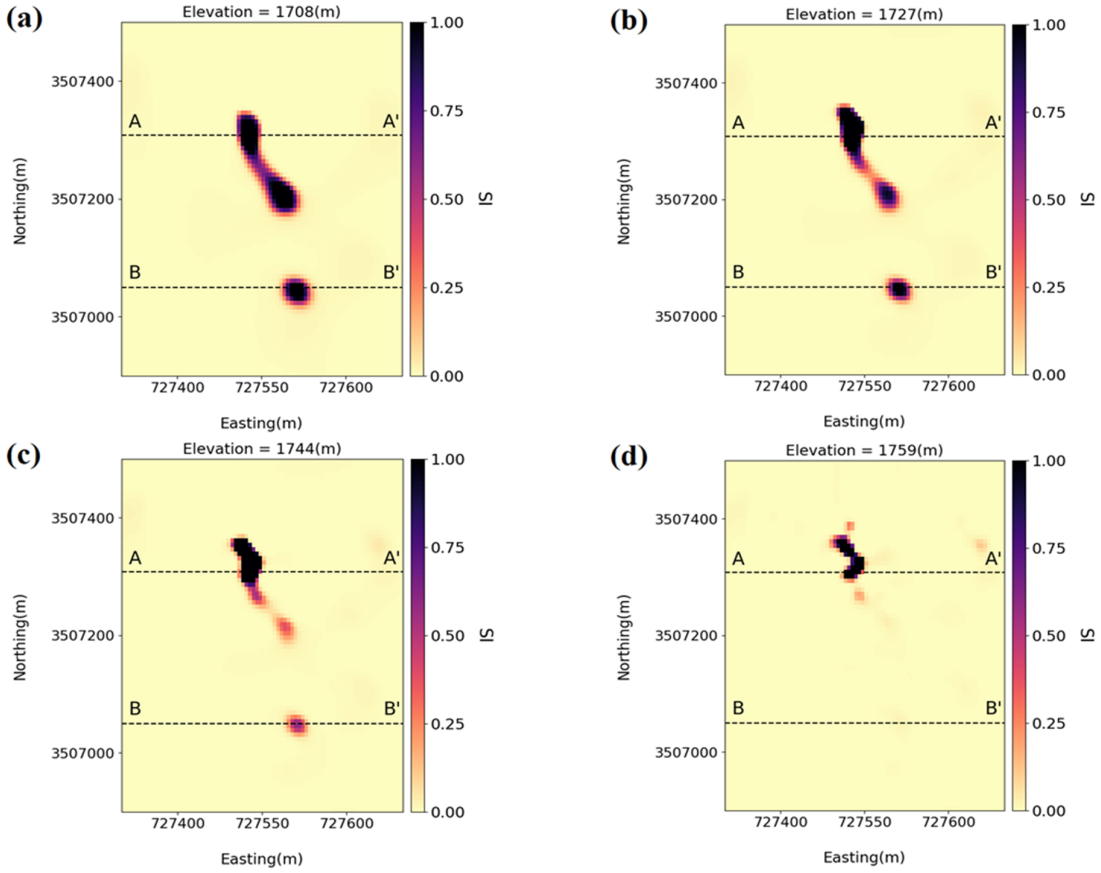

Figure 8. Plan view of the inversion results at different depths, revealing the distribution of the magnetized ore body. (a) Susceptibility model at elevation = 1708 m, (b) Elevation = 1727 m, (c) elevation = 1744 m, and (d) Elevation = 1759 m.

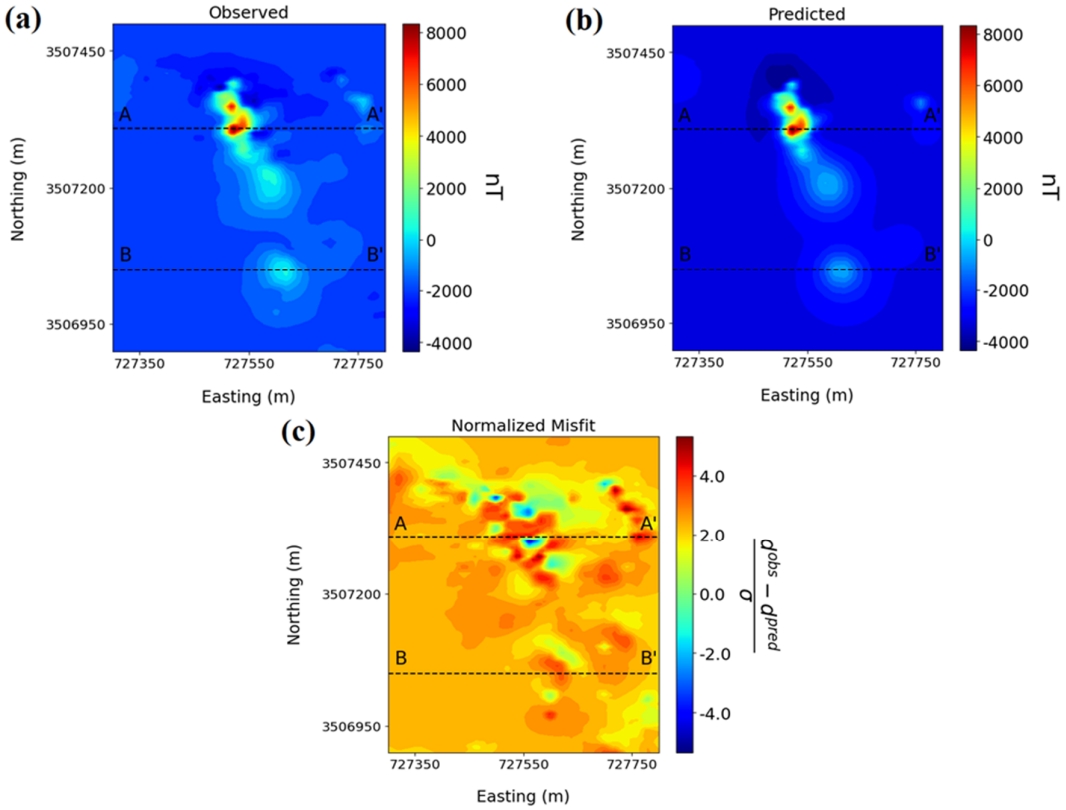

Figure 9. (a) Observed magnetic data after related corrections, (b) Calculated magnetic data after sparse norm inversion, (c) Normalized mis-fit map representing the weighted difference between the observed and calculated data.

The convergence curves presented in Figure 10 illustrate the behavior of the geophysical inversion process through iterations. The black curve, representing ϕ_d (data mis-fit), shows a rapid decrease from around 85,000 at iteration 0 to near zero by iteration 10, indicating a swift and effective reduction in data mis-fit. In contrast, the red curve, representing ϕ_m^p (model norm), starts close to zero and initially rises, peaking between iterations 12 and 15, before declining and stabilizing around 500 by iteration 25. This pattern suggests that the inversion process initially increases the model complexity to fit the data better but then refines the model to balance the data fit and complexity, avoiding overfitting. By iteration 25, both curves have stabilized, indicating that the inversion process has successfully converged, achieving a low data mis-fit and a controlled, plausible model complexity. This reflects an effective inversion process, where the algorithm efficiently fits the observed data, while maintaining a reasonable model complexity, demonstrating a successful convergence.

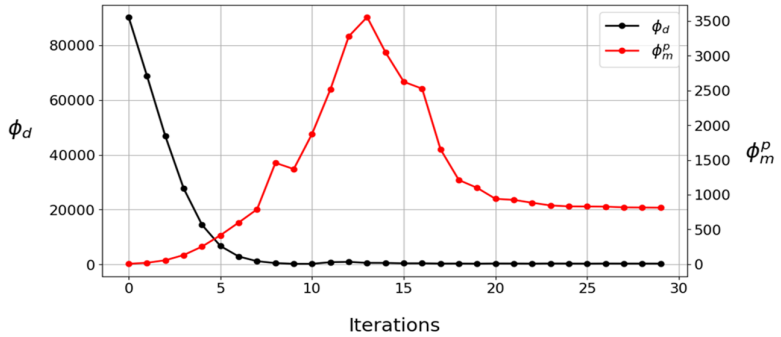

Figure 10. (a) Convergence curve for the case study Inversion. This plot depicts the progress of the susceptibility inversion for the Shavaz deposit. The x-axis represents the number of iterations completed during the inversion. The left y-axis shows the data mis-fit (ϕ_d), and its decrease after each iteration, indicating a better fit between the model and the observed data. The right y-axis represents the model norm (ϕ_m^p) and its variations, reflecting the complexity of the estimated subsurface model.

5. Geological Correlation

To validate the inversion results, we incorporate data from exploratory wells drilled within the studied area. A total of 24 wells were drilled at varying depths for detailed subsurface characterization [35]. These wells provided valuable geological and geochemical information including iron and iron oxide content, silicon dioxide (SiO_2) percentage, and phosphorite content inferred from P_2O_5 (phosphorus pentoxide) percentage [35]. While no boreholes were drilled directly within the geophysical target zones, Figure 11 presents the geological columns from two wells situated in a relatively close proximity.

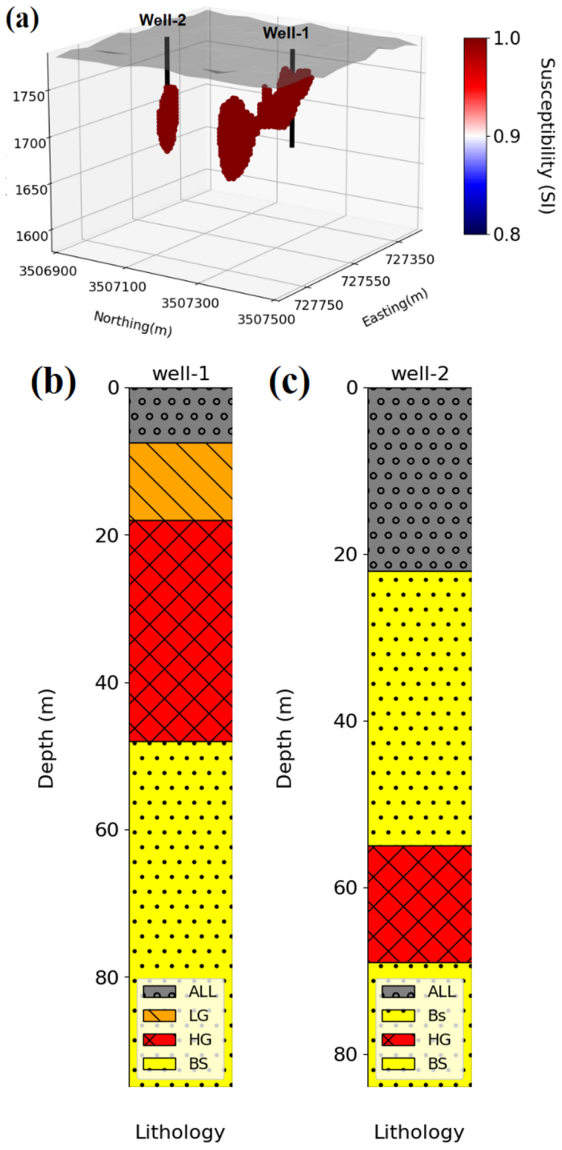

Figure 11. (a) 3D susceptibility model resulting from the inversion, showing the locations of the exploratory wells. (b) Lithological column at the coordinates (727545, 3507340). (c) Lithological column at the coordinates (727600, 3507030).

In Figure 11(a), we present a straightforward representation of the susceptibility contrast models obtained through inversion. We used a cut-off range of 0.8 SI to 1.0 SI to highlight the target magnetized area. The locations of the exploratory wells are also shown. Well-1 (Figure 11(b)), located at approximately (727545, 3507340), encountered a sequence starting with shallow alluvium sediments at the surface. This is followed by a thin layer of Low-Grade iron mineralization (LG) and a significant zone of a High-Grade iron mineralization (HG) with a thickness of about 28

meters. Barren units were observed below the high-grade mineralization zone. Well-2 (Figure 11(c)), situated near (727600, 3507030), revealed a thicker layer of alluvium sediments, compared to Well-1. Interestingly, Well-2 also showed a deeper and thinner zone of high-grade iron mineralization relative to Well-1 (with a thickness of about 18 meters). Although these observations were not obtained directly from the targeted geophysical zones, they exhibit a reasonable agreement with the inversion results presented in Figures 7 and 8. This alignment suggests that the inversion process successfully captured the general distribution and characteristics of the sub-surface iron mineralization, providing validation for its effectiveness.

6. Conclusions

This study investigated the effectiveness of three-dimensional sparse norm susceptibility inversion for characterizing the iron oxide-apatite deposits. We initially evaluated the method's performance using a well-defined synthetic model. Achieving satisfactory results on the synthetic model, we subsequently applied the inversion to the real-world case studied data. Firstly, the existing geophysical data underwent interpretation using various methods, leading to the approximate localization of potential mineralization zones. Following the inversion process, we visualized the resulting susceptibility models at various depths and cross-sections. The obtained inversion results were then validated using lithological columns constructed from the data acquired at two exploratory boreholes drilled near the target zones. The alignment between the inversion results and the well log data supported the success and reliability of the sparse norm susceptibility inversion methodology in the context of iron oxide-apatite exploration. However, for future studies aiming for potentially even more robust inversion and interpretation, employing a magnetization vector inversion technique is recommended.

Acknowledgment

The authors are grateful to the School of Mining Engineering, University of Tehran for their valuable support. They also extend their thanks to the Institute of Geophysics, University of Tehran for their valuable guidance in the field of inverse problems.

References

[1]. Oldenburg, D.W., & Pratt, D.A. (2002). Geophysical inversion for mineral exploration: A decade of progress in theory and practice. *Proceedings of Exploration, 7(5)*, 61-95.

[2]. Hammer, P.T.C., Hildebrand, J.A., & Parker, R.L. (1991). Gravity inversion using seminorm minimization: Density modeling of Jasper Seamount. *Geophysics, 56(1)*, 68-79.

[3]. Li, Y., & Oldenburg, D.W. (1996). 3-D inversion of magnetic data. *Geophysics, 61(1)*, 394-408.

[4]. Li, Y., & Oldenburg, D.W. (1998). 3-D inversion of gravity data. *Geophysics, 63(1)*, 109-119.

[5]. Li, Y., & Oldenburg, D.W. (2003). Fast inversion of large-scale magnetic data using wavelet transforms and a logarithmic barrier method. *Geophysical Journal International, 152(1)*, 251-265.

[6]. Oldenburg, D.W., & Li, Y. (2005). Inversion for applied geophysics: A tutorial. *Near-surface Geophysics, 5(1)*, 89–150.

[7]. Astic, T., & Oldenburg, D.W. (2018). Petrophysically guided geophysical inversion using a dynamic Gaussian mixture model prior. *SEG Technical Program expanded abstracts, 2018(1)*, 2312-2316.

[8]. Astic, T., & Oldenburg, D.W. (2019). A framework for petrophysically and geologically guided geophysical inversion using a dynamic Gaussian mixture model prior. *Geophysical Journal International, 219(3)*, 1989-2012.

[9]. Wang, K., & Yang, D. (2023). Joint inversion with petrophysical constraints using indicator functions, and the extended alternating direction method of multipliers. *Geophysics, 88(1)*, 49-64.

[10]. Lu, N., Liao, G., Xi, Y., Zheng, H., Ben, F., Ding, Z., & Du, L. (2021). Application of airborne magnetic survey in deep iron ore prospecting—A case study of Jinling area in tge Shandong Province, China. *Minerals, 11(10)*, 1041.

[11]. Milano, M., Varfinezhad, R., Bizhani, H., Moghadasi, M., Kalateh, A.N., & Baghzendani, H. (2021). Joint interpretation of magnetic and gravity data at the Golgohar mine in Iran. *Journal of Applied Geophysics, 195*, 104476.

[12]. Utsugi, M. (2019). 3-D inversion of magnetic data based on the L1–L2 norm regularization. *Earth, Planets and Space, 71(1)*, 73.

[13]. Liu, S., Hu, X., Zuo, B., Zhang, H., Geng, M., Ou, Y., Yang, T., & Vatankhah, S. (2020). Susceptibility and remanent magnetization inversion of magnetic data with a priori information of the Köenigsberger ratio. *Geophysical Journal International, 221(2)*, 1090-1109.

[14]. Rezayee, M.H., Khalaj, M., & Mizunaga, H. (2023). Structural analysis and susceptibility inversion

based on ground magnetic data to map the chromite mineral resources: A case study of the Koh Safi Chromite Ore Deposit, Parwan, Afghanistan. *Geoscience Letters, 10*, 43.

[15]. Liu, S., Hu, X., Zhang, H., Geng, M., & Zuo, B. (2017). 3D magnetization vector inversion of magnetic data: Improving and comparing methods. *Pure and Applied Geophysics, 174*, 1-24.

[16]. Fournier, D., Heagy, L.J., & Oldenburg, D.W. (2020). Sparse magnetic vector inversion in spherical coordinates. *Geophysics, 85(1)*, 33-49.

[17]. Shi, X., Geng, H., & Liu, S. (2022). Magnetization vector inversion based on amplitude and gradient constraints. *Remote Sensing, 14(21)*, 5497.

[18]. Karimzadeh, A., Abedi, M., & Norouzih, G. (2022). Potential field geophysical data fast imaging versus inverse modeling. *Geopersia, 12(1)*, 153-172.

[19]. Alamdar, K. (2016). Interpretation of the magnetic data from Shavaz iron ore using enhanced local wavenumber (ELW) and comparison with Euler deconvolution method. *Arabian Journal of Geosciences, 9(2)*, 144.

[20]. Alamdar, K. (2016). Stable downward continuation of potential field data using Tikhonov regularization for depth estimation of the mining bodies. *Iranian Journal of Geophysics, 10(2)*, 49-66.

[21]. Abedi, M. (2020). A focused and constrained 2D inversion of potential field geophysical data through Delaunay triangulation: A case study for iron-bearing targeting at the Shavaz deposit in Iran. *Physics of the Earth and Planetary Interiors, 309*, 106604.

[22]. Danaei, K., Moradzadeh, A., Norouzi, G.H., & Abedi, M. (2023). 3D inversion of magnetic data using Lanczos bidiagonalization and unstructured element. *International Journal of Mining and Geo-Engineering, 57(1)*, 89-99.

[23]. Cockett, R., Kang, S., Heagy, L.J., Pidlisecky, A., & Oldenburg, D.W. (2015). SimPEG: An open-source framework for simulation and gradient-based parameter estimation in geophysical applications. *Computers & Geosciences, 85*, 142–154.

[24]. Ardestani, V.E., Fournier, D., & Oldenburg, D.W. (2022). A localized gravity modeling of the upper crust beneath Central Zagros. *Pure and Applied Geophysics, 179(9)*, 2365–2381.

[25]. Sharma, P. V. (1966). Rapid computation of magnetic anomalies and demagnetization effects caused by bodies of arbitrary shape. *PAGEOPH, 64*, 89–109.

[26]. Fournier, D., Oldenburg, D.W., & Davis, K. (2016). Robust and flexible mixed-norm inversion. *SEG Technical Program Expanded Abstracts, 2016*, 1542–1547.

[27]. Fournier, D., & Oldenburg, D.W. (2019). Inversion using spatially variable mixed L_p-norms. *Geophysical Journal International, 218(1)*, 268–282.

[28]. Rezayee, M.H., Akbar, A.Q., Poyesh, T., Rawnaq, E., Samim, K.M., & Mizunaga, H. (2023). 3D geophysical modeling based on multi-scale edge detection, magnetic susceptibility inversion, and magnetization vector inversion in Panjshir, Afghanistan, to detect probabilistic Fe-polymetallic bearing zones. *Geosciences, 13(12)*, 376.

[29]. Li, Z., Yao, C., Zheng, Y., Wang, J., & Zhang, Y. (2018). 3D magnetic sparse inversion using an interior-point method. *Geophysics, 83(1)*, 15–32.

[30]. Teimouri, S., Ghorbani, M., Shinjo, R., & Modabberi, S. (2023). Geology and geochemistry of metasomatite rocks associated with Kiruna iron oxide apatite and the evolution of fluids responsible for metasomatism in Choghart and Chadormalu deposits (Bafq mining district, Central Iran). *Arabian Journal of Geosciences, 16*, 238.

[31]. Berberian, M., & King, G.C.P. (1981). Towards a paleogeography and tectonic evolution of Iran. *Canadian Journal of Earth Sciences, 18(2)*, 210-265.

[32]. Mehdipour Ghazi, J., & Moazzen, M. (2023). Cadomian iron ore bodies in the Bafq-Saghand metallogenic province, Iran: Genetic constraints from field observations and laser ablation ICP-MS mineral studies. *International Geology Review, 66(5)*, 1144–1164.

[33]. Heidarian, H., Lentz, D.R., Alirezaei, S., McFarlane, C.R.M., & Peighambari, S. (2018). Multiple Stage Ore Formation in the Chadormalu Iron Deposit, Bafq Metallogenic Province, Central Iran: Evidence from BSE Imaging and Apatite EPMA and LA-ICP-MS U-Pb Geochronology. *Minerals, 8(3)*, 87.

[34]. Ghanbarifar, S., Hosseini, S. H., Abedi, M., & Afshar, A. (2024). A dynamic window-based Euler depth estimation algorithm for potential field geophysical data. *Bulletin of Geophysics and Oceanography, 65*, 399-438.

[35]. Sadraeifar, B., & Abedi, M. (2024). Innovative imaging of iron deposits using cross-gradient joint inversion of potential field data with petrophysical correlation. *Near Surface Geophysics, 22(6)*, 553–573.

[36]. Ghanbarifar, S., Hosseini, S.H., Ghiasi, S.M., Abedi, M., & Afshar, A. (2024). Joint Euler deconvolution for depth estimation of potential field magnetic and gravity data. *International Journal of Mining and Geo-Engineering, 58(2)*, 121-134.

وارون سازی سه بعدی و تفسیر داده های مغناطیسی زمینی برای آشکارسازی منابع آهن: مطالعه موردی سنگ آهن شاواز در ایران

بردیا صدرائی‌فر[1]، میثم عابدی[2*]، و سیدحسین حسینی[1]

۱- موسسه ژئوفیزیک، دانشگاه تهران، تهران، ایران

۲- دانشکده مهندسی معدن،دانشکدگان فنی، دانشگاه تهران، تهران، ایران

ارسال ۲۰۲۴/۰۶/۲۰، پذیرش ۲۰۲۴/۱۱/۳۰

* نویسنده مسئول مکاتبات: maysamabedi@ut.ac.ir

چکیده:

نهشته آهن شاواز، واقع در جنوب‌غربی استان یزد در بلوک ایران مرکزی، نزدیک به کمربند متالوژنی بافق، یک منبع مهم و اقتصادی از اکسید آهن-آپاتیت است. این نهشته اغلب شامل هماتیت و مقداری کمی مگنتیت بوده که از طریق مطالعات ژئوفیزیکی میدان پتانسیل قابل شناسایی می باشد. هدف این مطالعه آشکارسازی کانه زایی مگنتیت در این نهشته با استفاده از وارون‌سازی مقید شده خودپذیری مغناطیسی می‌باشد. ابتدا یک مدل مصنوع چندمنبعی با سه مکعب یکسان در عمق‌های مختلف شبیه‌سازی شد تا رویکرد وارون‌سازی نُرم پراکنده ارزیابی شود. سپس این روش پس از اصلاحات ضروری داده‌های مغناطیسی به مطالعه موردی اعمال شد. همچنین به‌منظور ارتقاع تفسیر ناهنجاری‌های مغناطیسی باقی‌مانده و دستیابی به بینشی دقیق تر در مورد نقاط کانه زایی و عمق آن ها، از روش های سیگنال تحلیلی و ادامه فراسو استفاده شده است. نتایج وارون‌سازی در مقاطع مختلف نشان داد که دو کانه زایی مگنتیت عدسی شکل و کم‌عمق با گستردگی عمودی متوسط ۶۰ متر وجود دارد. قابل‌توجه است که یکی از توده های مگنتیتی به علت تاثیر گسل دهشیر-بافت حدود ۳۰ متر عمیق‌تر قرار دارد. مقادیر کم، انطباق نرمال‌شده، موفقیت در کمینه کردن تابع هدف در طول وارون‌سازی را تایید کرد. علاوه‌براین، مدل‌های خودپذیری مغناطیسی با مطالعات زمین‌شناسی قبلی و داده‌های چاه های اکتشافی هم‌راستا هستند که کارایی الگوریتم وارون‌سازی نُرم پراکنده را نشان می‌دهند.

کلمات کلیدی: شاواز، مگنتیت، وارون سازی خودپذیری مغناطیسی، مدل مصنوع، سیگنال تحلیلی، ادامه فراسو.